Soft Matter

PAPER

View Article Online
View Journal | View Issue

Cite this: *Soft Matter*, 2017, 13, 486

Ordering block copolymers with structured electrodes

Ulrich Welling and Marcus Müller*

We study the kinetics of alignment and registration of block copolymers in an inhomogeneous electric field by computer simulations of a soft, coarse-grained model. The two blocks of the symmetric diblock copolymers are characterized by different dielectric constants. First, we demonstrate that a combination of graphoepitaxy and a homogeneous electric field extends the maximal distance between the topographical guiding patterns that result in defect-free ordering compared to graphoepitaxy alone. In a second study, the electric field in the thin block copolymer film is fabricated by spatially structured electrodes on an isolating substrate arranged in a one-dimensional periodic array; no additional topographical guiding patterns are applied. The dielectrophoretic effect induces long-range orientational order of the lamellae and, additionally, registers the lamellar structure with the electrodes due to the field inhomogeneities at the edges of the structured electrodes. Thus, orientational and translational order is established by the inhomogeneous electric field. The simulations identify a process protocol of time-dependent electric potentials that suppresses defect formation by initially forming a sandwich-like structure and subsequently reorienting these lying into standing lamellae that are registered with the structure of the electrodes. This process-directed self-assembly results in large defect-free arrays of aligned and registered lamellae using electrodes with a saw-tooth period of 4 lamellar periodicities, L_0, and a spacing of $10L_0$.

Received 18th August 2016,
Accepted 2nd December 2016

DOI: 10.1039/c6sm01911k

www.rsc.org/softmatter

1 Introduction

Directed self-assembly (DSA) of block copolymer (BCP) materials is considered as a promising strategy for extending the capabilities of lithographic methods to the sub-10 nm range. The amphiphilic architecture of BCPs prevents macroscopic phase separation and, instead, the thermodynamically incompatible components spontaneously form periodic nanostructures.[1,2] Chemical or topographic guiding patterns direct this self-assembly into technologically useful structures like lines and spaces. In the former situation – chemoepitaxy[3,4] – one employs a chemical stripe pattern, whose periodicity is commensurate bulk lamellar period, L_0 of the symmetric BCP to direct the self-assembly.[5] In the latter strategy – graphoepitaxy[6–10] – topographic trenches on the substrate are used to align and register the BCP morphology. Much current scientific effort focuses on optimizing copolymer materials and guiding strategies to obtain dense, defect-free structures over large areas and in registration with outer boundaries.[11–14,17–21] In both cases, chemoepitaxy and graphoepitaxy, the characteristic length scale of the guiding pattern is restricted to a small integer multiple, n = 3–6, of the BCP periodicity, L_0. This density multiplication factor, n, is dictated by the finite range, ξ, over which the edges of the guiding pattern – boundaries between chemical stripes or walls of trenches – influence the kinetics of structure formation in the BCP material.

In contrast to these short-range, chemical or topographic guiding fields, shear flow[14–16,22–31] or electric fields[32–48] are well known for controlling the orientation of the BCP morphology over large scales. By virtue of the long-range character of shear or electric fields, pervading the entire sample volume, the field-generating sheared boundaries or electrodes can be many L_0 spaced apart. Unfortunately, however, homogeneous long-range fields typically do not give rise to registration of the morphology with outer boundaries.

Here we explore the opportunities that electric-field effects with or without combination of graphoepitaxy offer for aligning and registering the BCP morphology. In the next section, Section 2, we describe our soft, coarse-grained model of BCPs in an inhomogeneous electric field. In Section 3 we demonstrate that the combination of graphoepitaxy and electric-field effect allows the fabrication of defect-free, registered lines-and-spaces structures in wide trenches. Section 4 discusses how an inhomogeneous electric field aligns and registers the BCP morphology and, in Section 5, we extend this strategy to electrodes that are structured with a larger period than L_0 by judiciously choosing an assembly protocol. A brief summary and outlook conclude our manuscript.

Institut für Theoretische Physik, Georg-August-Universität, 37077 Göttingen, Germany. E-mail: mmueller@theorie.physik.uni-goettingen.de

2 Soft, coarse-grained model and simulation techniques

We employ a highly coarse-grained model for dense BCP melts. n block copolymers are confined into a thin film with dimensions $L_x \times L_y \times L_z$. The top and bottom surface of the film, representing the supporting substrate and vacuum, are represented as impenetrable hard walls that exert no preference for any block, A or B. Periodic boundary conditions are applied in the two lateral directions, x and y.

Each linear chain molecule is represented by $N = 32$ coarse-grained interaction centers (beads), which are connected by harmonic springs.[49,50]

$$\frac{\mathscr{H}_{\mathrm{b}}}{k_{\mathrm{B}}T} = \sum_{i=1}^{n}\sum_{s=1}^{N-1}\frac{3(N-1)}{2{R_{\mathrm{e0}}}^2}[\mathbf{r}_i(s)-\mathbf{r}_i(s+1)]^2. \tag{1}$$

with R_{e0} being the mean-squared end-to-end distance of a Gaussian chain in the absence of any other interactions than the bonded Hamiltonian, eqn (1). R_{e0} sets the unit of length. $\mathbf{r}_i(s)$ denotes the position of the sth coarse-grained segment of polymer i, and n denotes the number of polymer chains.

The non-bonded interactions, $\mathscr{H}_{\mathrm{nb}}$, consist of a soft segment repulsion, characterized by the inverse isothermal compressibility κN, the repulsion of unlike blocks, parameterized by the Flory–Huggins parameter χN, and the energy of the electric field, $\mathscr{H}_{\mathrm{el}}$.

$$\frac{\mathscr{H}_{\mathrm{nb}}}{k_{\mathrm{B}}T} = \frac{\rho_0{R_{\mathrm{e0}}}^3}{N}\int\frac{\mathrm{d}\mathbf{r}}{{R_{\mathrm{e0}}}^3}\left\{\frac{\kappa N}{2}\left[\hat{\phi}_{\mathrm{A}}(\mathbf{r})+\hat{\phi}_{\mathrm{B}}(\mathbf{r})-1\right]^2 - \frac{\chi N}{4}\left[\hat{\phi}_{\mathrm{A}}(\mathbf{r})-\hat{\phi}_{\mathrm{B}}(\mathbf{r})\right]^2\right\}+\frac{\mathscr{H}_{\mathrm{el}}}{k_{\mathrm{B}}T} \tag{2}$$

where ρ_0 denotes the segment number density, and $\bar{N} \equiv \left(\frac{\rho_0{R_{\mathrm{e0}}}^3}{N}\right)^2$ is the invariant degree of polymerization. In our simulations we use $\bar{N} = 209^2$, which corresponds to a typical value of a BCP melt.

The first term restrains fluctuations of the total density and in accord with previous studies we set $\kappa N = 50$. The second term describes the repulsive interaction between unlike segment species, A and B, giving rise to microphase separation. In the following we use the incompatibilities, $\chi N = 18$ and $\chi N = 25$. Calculations of the minimum free-energy path using self-consistent field theory[51] demonstrate that the free-energy barrier of the annihilation of tight dislocation pairs in lamellar copolymer films vanishes at around $\chi N = 18$ whereas defects are metastable at $\chi N = 25$. The inverse compressibility $\kappa N \approx 2\chi N$ is chosen to allow density fluctuations on the same energy scale as those resulting from the repulsion of unlike segments; the value suffices to suppress density fluctuations on the length scale of a small fraction of the polymer size, R_{e0}.

$\hat{\phi}_{\mathrm{A}}(\mathbf{r})$ represents the normalized, microscopic density of A segments at position $\mathbf{r}$ and it is related to the particle coordinates *via*

$$\hat{\phi}_{\mathrm{A}}(\mathbf{r}) = \frac{1}{\rho_0}\sum_{i=1}^{n}\sum_{s=1}^{Nf}\delta[\mathbf{r}-\mathbf{r}_i(s)] \tag{3}$$

where $f = 1/2$ denotes the fraction of A segments on a BCP. A similar expression holds for the local, microscopic density of B segments, $\hat{\phi}_{\mathrm{B}}(\mathbf{r})$. Expressing $\hat{\phi}_{\mathrm{A}}$ and $\hat{\phi}_{\mathrm{B}}$ through the particle coordinates the non-bonded Hamiltonian is a function of the configuration, $\{\mathbf{r}_i(s)\}$, suitable for particle-based computer simulations. In order to regularize the δ-function in eqn (3), we compute the densities and other spatially dependent quantities on a collocation grid by assigning a particle to the nearest grid point. The spacing of the collocation grid, ΔL, is commensurate with the natural period of the copolymer, so that $L_0 = 12\Delta L$. This discretization is sufficiently fine to spatially resolve the internal AB interfaces between block copolymer domains in our soft, coarse-grained model, and it is sufficiently coarse for the quasi-instantaneous field approximation that is invoked by the single-chain-in-mean-field algorithm be accurate.[49] For the incompatibilities used in this manuscript, the bulk lamellar spacing, as estimated from the isotropy of the bonded single-chain stress, is $L_0 = 1.558R_{\mathrm{e0}}$ and $L_0 = 1.677R_{\mathrm{e0}}$, respectively, in the absence of an electric field.

The electric energy, $\mathscr{H}_{\mathrm{el}}$, is calculated from the solution of the electric field, $\mathbf{E} = -\nabla\psi$

$$\mathscr{H}_{\mathrm{el}} = -\frac{1}{2}\int\mathrm{d}\mathbf{r}\varepsilon(\mathbf{r})|\nabla\psi(\mathbf{r})|^2 \tag{4}$$

$\varepsilon(\mathbf{r})$ is the permittivity that depends on the position *via* the local composition. The electric potential, $\psi(\mathbf{r})$, is the solution of the Laplace equation

$$\nabla[\varepsilon(\mathbf{r})\nabla\psi(\mathbf{r})] = 0 \tag{5}$$

We use a constitutive equation to relate the local permittivity to the local composition

$$\varepsilon(\mathbf{r}) = \varepsilon_0\frac{\varepsilon_{\mathrm{A}}\hat{\phi}_{\mathrm{A}}(\mathbf{r})+\varepsilon_{\mathrm{B}}\hat{\phi}_{\mathrm{B}}(\mathbf{r})}{\hat{\phi}_{\mathrm{A}}(\mathbf{r})+\hat{\phi}_{\mathrm{B}}(\mathbf{r})} \tag{6}$$

where ε_0 is the vacuum permittivity, and ε_{A} and ε_{B} are the dielectric constants of the two segment species, A and B, respectively. In our simulation, the dielectric constants of the two polymer domains are set to $\varepsilon_{\mathrm{A}} = 2$ and $\varepsilon_{\mathrm{B}} = 5$. This dielectric contrast is close to the one of typical copolymer components, for example the dielectric contrast of PS-block-PMMA is around $1.2\varepsilon_0$ (PS $\varepsilon = 2.5\varepsilon_0$, PMMA $\varepsilon = 3.7\varepsilon_0$).[52] The dielectric constant of the vacuum above the BCP film is unity, whereas the dielectric constant of the supporting substrate is $\varepsilon_{\mathrm{s}} = 2$ and, for selected parameters, we have also employed the larger value, $\varepsilon_{\mathrm{s}} = 11$ but observed no change in the kinetic pathway of structure alignment.

The statistical mechanics of this model is studied by Single-Chain-in-Mean-Field (SCMF) simulations[49,53,54] that exploit the separation between the strong bonded and weak non-bonded forces by temporarily substituting the weak non-bonded interactions by fields, $w_{\mathrm{A}}(\mathbf{r})$ and $w_{\mathrm{B}}(\mathbf{r})$, acting on A and B segments,

respectively. The segment positions are updated by Smart Monte-Carlo moves using the force of the strong bonded interaction to propose a trial displacement.[55,56] These local random displacements give rise to Rouse-like dynamics.[57] The chain relaxation time, τ, characterizes the time that the center of mass of a macromolecule requires to diffuse its end-to-end distance $R_e = \sqrt{\langle \mathbf{R}_e^2 \rangle} = 1.02 R_{e0}$ and it takes the value $\tau = R_e^2/D =$ 9711 Monte Carlo-steps in a disordered state, $\chi N = 0$. The slight difference between the end-to-end distance, R_e, in a melt and the value, R_{e0}, of non-interacting chain molecules arises from the soft repulsions of strength κ, restraining density fluctuations.

In the present study, the fields, $w_A(\mathbf{r})$ and $w_B(\mathbf{r})$, also include the electrostatic interactions.[48] After each Monte-Carlo step, during which each particle has had the chance to be moved once on average, the quasi-instantaneous fields are re-calculated from the particle-densities according to[48,49]

$$\begin{aligned}\frac{w_A(\mathbf{r})N}{k_B T} &\equiv \frac{N}{\rho_0 k_B T}\frac{\delta \mathscr{H}_{nb}}{\delta \hat{\phi}_A(\mathbf{r})} \\ &= \kappa N\left[\hat{\phi}_A(\mathbf{r}) + \hat{\phi}_B(\mathbf{r}) - 1\right] - \frac{\chi N}{2}\left[\hat{\phi}_A(\mathbf{r}) - \hat{\phi}_B(\mathbf{r})\right] \\ &\quad - \frac{\varepsilon_0(\varepsilon_A - \varepsilon_B)N}{2\rho_0 k_B T}\frac{\hat{\phi}_B(\mathbf{r})}{\left[\hat{\phi}_A(\mathbf{r}) + \hat{\phi}_B(\mathbf{r})\right]^2}|\nabla\psi(\mathbf{r})|^2\end{aligned} \quad (7)$$

and a similar expression holds for the field, w_B, that acts on a B segment. If E_0 denotes the typical change of the electric potential on the scale R_e, we estimate the strength of the electric contribution to w_A as follows

$$\begin{aligned}w_A^{el}(\mathbf{r}) &= -\frac{\varepsilon_0 E_0^2(\varepsilon_A - \varepsilon_B)}{2\rho_0}\frac{\hat{\phi}_B(\mathbf{r})}{\left[\hat{\phi}_A(\mathbf{r}) + \hat{\phi}_B(\mathbf{r})\right]^2}\left|\frac{\nabla\psi(\mathbf{r})}{E_0}\right|^2 \\ &\sim -\frac{\varepsilon_0}{4\rho_0}(\varepsilon_A - \varepsilon_B)E_0^2\end{aligned} \quad (8)$$

i.e., the dielectrophoretic force, $-\nabla w_A^{el} \sim \frac{\varepsilon_0}{4\rho_0}(\varepsilon_A - \varepsilon_B)\nabla E_0^2$ attracts the component with the larger dielectric constant to regions of high field strength.

The typical strength of non-bonded interactions is $w_A^{\chi} \sim k_B T\chi$. Thus, we estimate the relative strength of the effect of the electric field by

$$\frac{w_A^{el}}{w_A^{\chi}} \sim \frac{(\varepsilon_A - \varepsilon_B)}{\chi N\sqrt{\mathscr{N}}} \cdot \frac{\varepsilon_0 R_e}{k_B T} \cdot (R_e E_0)^2 \quad (9)$$

This relation motivates the definition of a normalized electric potential, $\tilde{\psi}(\mathbf{r}) \equiv \sqrt{\frac{\varepsilon_0 R_e}{k_B T}}\psi(\mathbf{r})$. In our simulations, this dimensionless parameter, $\tilde{\psi}$, adopts values in the range $0 \le |\tilde{\psi}| \le 70$, and the corresponding homogeneous electric field typically is in the range $E_0 \sim \frac{|\tilde{\psi}|}{R_e} \le 4$. For the systems with strong inhomogeneities, however, the electric field can be locally larger.

3 Combining graphoepitaxy with a homogeneous electric field

First, we consider the combination of graphoepitaxy and electric-field effect. The BCP system is confined into a trench with neutral walls in z-direction, which represent the substrate and the free surface of the BCP film. The film thickness, $L_z = 0.66L_0$, is chosen as to frustrate lying structures. The side walls at $x = 0$ and $x = L_x = 11L_0$ attract the A component with a potential

$$\frac{V_{wall}}{k_B T} = 0.25 \quad (10)$$

that extends over a distance $L_0/12$. In the y-direction, $L_y = 11L_0$ the system is terminated by electrodes that are hard and impenetrable but do not exhibit any preference for the A or B blocks. This set-up is sketched in the left panel of Fig. 1.

In the absence of an electric field, this set-up corresponds to graphoepitaxy in a trench with preferential side walls. The side walls break the translational symmetry along the x-direction and direct the formation of a half-lamella of the preferred component, A, at the two side walls. This topographic guiding

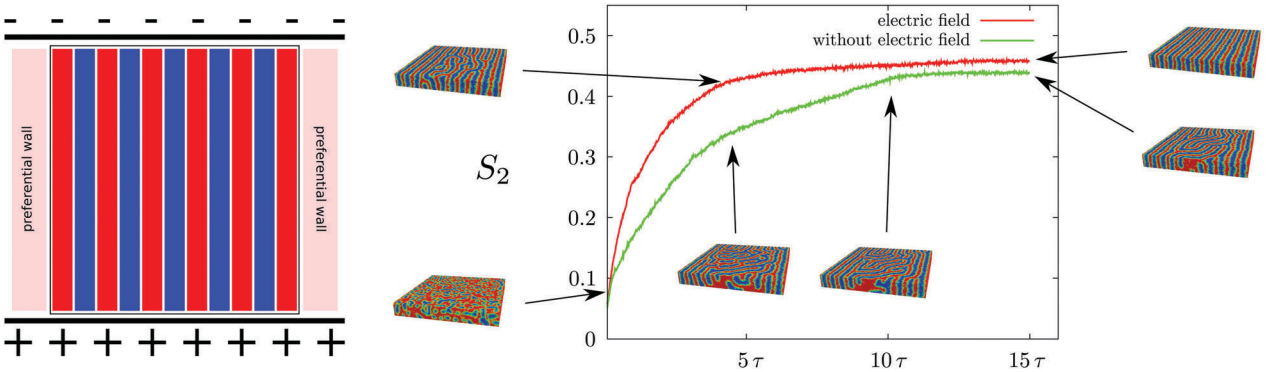

Fig. 1 Defect-free alignment of a BCP film confined between selective side walls (graphoepitaxy) with an orthogonal electric field. (left) Sketch of the system geometry. The electric field in the side walls is constant in time. (right) Single-chain orientational order parameter, S_2, as a function of time with and without an electric field. The snapshots illustrate the kinetics of structure formation at various times, $t/\tau = 0.1$, 1, 0, and 15, after the quench from the disordered structure. For visual clarity the composition depicted in the snapshots has been averaged over $\Delta t = 0.001\tau$, reducing local fluctuations.

field aims at registering and aligning the lamellae across the entire x-direction as the system is quenched from the disordered state, $\chi N = 0$, to the microphase-separated state at incompatibility $\chi N = 25$. The snapshots in Fig. 1 reveal, however, that only 2 additional, registered and aligned, lamellar domains are formed in the course of structure formation, whereas defects occur in the middle between the two guiding side walls. This observation in our simulation study is consistent with graphoepitaxy experiments where the ordering influence of a preferential side wall often is insufficient to fabricate defect-free lamellar structures in a wide trench.[6,8,58]

To quantify the degree of smectic order, we monitor the largest eigenvalue, S_2, of the tensor defined by dyadic product of the single-chain end-to-end vector. The value $S_{2,\max} = 1/2$ indicates perfect alignment of the end-to-end vector $\mathbf{R}_e$ of each chain in the same direction. The time evolution of this order parameter, $S_2(t)$, is presented in the right panel of Fig. 1. Within a relaxation time, τ, after the quench from the disordered phase, microphase-separated domains are formed and the order parameter increases up to about 10τ. Subsequent changes of the morphology are protracted and no defect-free order is established within 15τ. Presumably the system has reached a metastable state and thermally activated processes are required to annihilate the remaining defects at $\chi N = 25$.[51,59]

In order to enhance graphoepitaxy we apply a homogeneous orthogonal electric field along the y-direction. To reduce the computational effort of solving the electric field, the boundary values of $\tilde{\psi}$ at the preferential walls in the x-direction, $x = 0L_0$ and $x = 11L_0$, and at the neutral walls in z-direction are set to the homogeneous solution of the electric field in a plate capacitor. This approach follows the strategy applied for the simulation of copolymers in cylindrical slabs.[48] The potential applied to the electrodes is $\pm 16\tilde{\psi}$, corresponding to an electric field of $2.9\tilde{\psi}/L_0$. The simulations start from the disordered state, $\chi N = 0$, and are quenched below the order–disorder transition, $\chi N = 25$. Simultaneously the electric field is switched on and the nearly homogeneous electric field along the y-direction creates a torque on the AB domain interfaces, leading to an alignment of the interfaces parallel to the electric field.

The right panel of Fig. 1 presents snapshots of the time evolution and the order parameter for this combination of topographic and electric guiding fields. This combination results in defect-free assembly in a wide trench, $L_x = 11L_0$, and also accelerates the ordering kinetics. In fact, the defect-free state is established at $t = 12.5\tau$ suggesting that electric field significantly contributes to defect removal by lowering the barriers for the annihilation of misaligned defect structures. The time dependence of the order parameter with a field above the critical ordering strength is rather continuous, suggesting that the barriers encountered in the course of structure formations do not significantly exceed the thermal energy scale, k_BT. This first example illustrates that the combination of two orthogonal fields – the topographic side walls that locally register the A lamellae and the long-range electric field that dictates the overall orientation of the smectic structure – can significantly extend the process window of defect-free graphoepitaxy towards wider trenches and accelerated ordering kinetics.

Fig. 2 System with two structured electrodes $30L_0 \times 6L_0 \times 3L_0/4$: the electrodes are shown in solid blue and red color, whereas equipotential surfaces are depicted by semi-transparent, colored surfaces. The potential values are equally spaced so that the spatial distance between equipotential surfaces is inversely proportional to the strength of the electric field, $\mathbf{E} = -\nabla\psi$. The structured electrodes have a periodicity L_0 in y-direction and a width $L_0/2$ along the x-axis. In the middle of the film between the electrodes the field is nearly homogeneous, whereas the electrode edges result in a significant enhancement of the local field.

4 Film on top of a patterned electrode

In this section we explore if an inhomogeneous field is able to register the lamellae to a specified position in addition to its orientation effect. To this end, we consider two parallel, structured electrodes that are buried inside the insulating substrate, $\varepsilon_s = 2$, directly below the BCP film, *i.e.* the bottom surface of the BCP film is flat and the electrodes do not provide any topographic cues that direct the structure formation. The two electrodes are spaced a distance $L_x/2 = 15L_0$ apart. A description of solving the Laplace equation, eqn (5), in this thin-film geometry is provided in the Appendix.

The system geometry and the electric potential are presented in Fig. 2. In the middle of the film between the two parallel electrodes, the field is approximately homogeneous and the concomitant torque tends to align the normals of the lamellae parallel to the yz plane. The geometric confinement into a thin film breaks this yz degeneracy because the chosen film thickness, $L_z = 3L_0/4$, maximally frustrates lying lamellar structures (with normals in the z-direction). Thus the combination of homogeneous electric field and film thickness favors the formation of standing lamellae with normals along the y-direction in the middle between the electrodes, *i.e.*, the orientational symmetry is broken.

The electrode structure is periodic along the y-direction, matching the domain spacing, L_0, of the BCP. As shown in Fig. 2, there is a pronounced local enhancement of the electric field at the edges of the structured electrodes. The high value of the local field strength gives rise to a dielectrophoretic force that attracts the component, B, with the larger dielectric constant. Thus, the enhancement of the magnitude of the electric field acts similar to a substrate preference in chemoepitaxy – the strength of this attraction being tunable by the applied voltage between the electrodes.

Therefore the structure of the electrodes breaks the translational invariance along the y-direction. Since the periodicity of the electrodes and of the concomitant local enhancement of the field magnitude along the y-direction coincides with lamellar spacing, L_0, of the block copolymer, we expect that the lamellar structure will locally register with the edges of the electrodes.

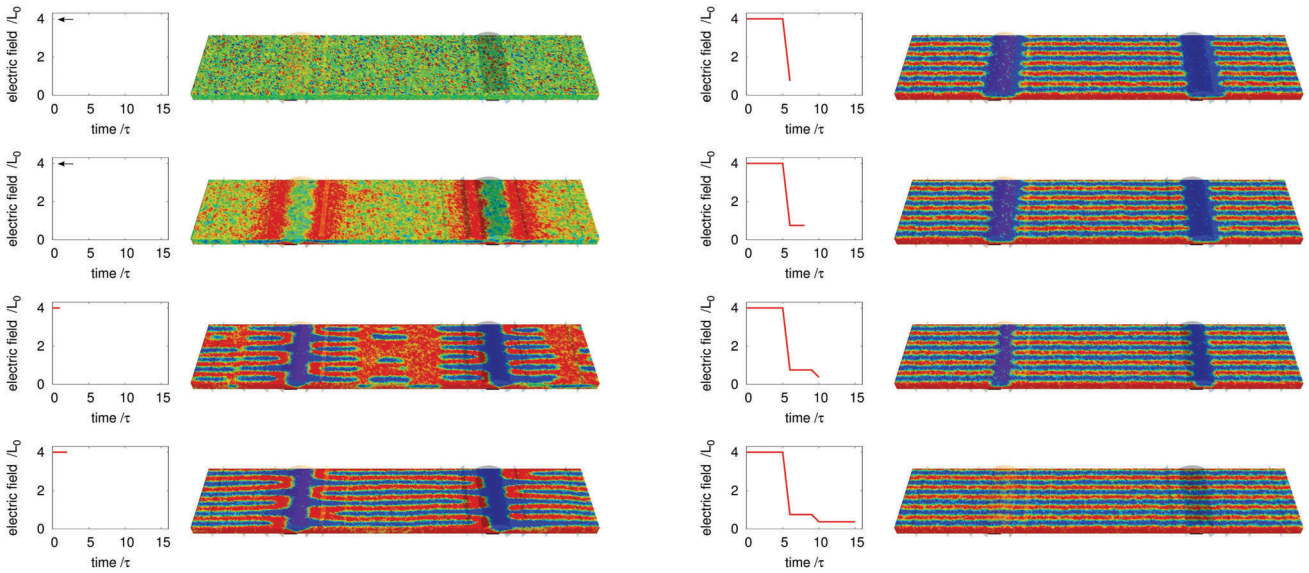

Fig. 3 BCP ordering kinetics by structured electrodes with a time-dependent potential. This process-directed self-assembly results in a defect-free lamellar structure, in which the lamellae are aligned and register with the edges of the electrodes. Initially, the electric field leads to lying sandwich structure, where the high-ε component segregates to the film surfaces. Subsequently, this orientation is overturned to the favored standing lamellae. This process starts at the electrodes, where the morphology is registered with the edges of the electrodes and propagates into the middle of the film. Right on top of the electrodes, however, the lying structure is stabilized by the electric field. Finally, the field strength is reduced to allow the lamellae on the electrodes to be replaced by the standing lamellae and form a fully aligned and registered lamellar film. The snapshots are taken at the times $t = 0\tau$, $t = 0.001\tau$, $t = 1\tau$, $t = 2\tau$, $t = 6\tau$, $t = 8\tau$, $t = 10\tau$ and $t = 15\tau$ as indicated in the plot to the left of the configurations. For the first two snapshots an arrow in the plot indicates the field strength. The snapshots for $t \leq \tau$ are averaged for visual clarity over a duration of $\Delta t = 0.001\tau$.

The ordering pathway is presented in Fig. 3; it can be divided in three stages that we discuss in turn:

(i) BAB-sandwich structure

The simulation starts in the disordered state and, at time $t = 0$, the incompatibility is increased to $\chi N = 25$ and a field (of strength $4\tilde{\psi}/L_0$ in the middle between the electrodes) is applied. In the very initial stage, $0 \leq t \leq 0.1\tau$, the electric field gives rise to a fast process, during which the copolymer forms a BAB sandwich structure. The component, B, of higher dielectric constant segregates towards the bottom and the top of the thin film, whereas the low-ε component, A, is enriched at the center of the film, $z \approx L_z/2$. This initial, fast ordering process is caused by two effects: first, the kinked edges of the structured electrode give rise to strong field inhomogeneities that attract one component of the copolymer. An additional, weaker effect occurs on the top surface of the film, particularly in the vicinity of the electrodes. In this region, the component of the field, E_z, perpendicular to the surface passes from the copolymer material with an average dielectric constant of 3.5 into vacuum 1, giving rise to a field inhomogeneity. In the simulation, this surface effect only affects the top discretization layer of width, ΔL. Although our soft, coarse-grained model cannot faithfully represent the sharp density profile of a polymer film in coexistence with its vapor phase,[50,60] also in an experimental polymer film, the continuously changing density at the free surface will give rise to a variation of the dielectric constant at the free surface and a concomitant dielectrophoretic force. Adjusting the applied potentials, one will be able to attract the copolymer material with the higher dielectric constant to the film surfaces in an experimental setup.

(ii) Standing, aligned and registered lamellae between electrodes

The film thickness, $L_z = 3L_0/4$ highly frustrates this initial BAB sandwich structure. Thus, starting from the vicinity of the electrodes, this initial structure begins to reorient into standing lamellae for $t > 2\tau$. These standing lamellae are registered with the edges of the structured electrodes due to the dielectrophoretic force in the inhomogeneous field. These registered standing lamellae propagate away from the electrodes along the x-direction, replacing the initial, frustrated BAB sandwich morphology. The orientation of these standing lamellae is stabilized by the homogeneous electric field in the middle between the two electrodes and the geometric confinement into a thin film. The two, registered and aligned, lamellar grains that emerge from each electrode merge in the middle between the electrodes, forming a defect-free, registered and aligned, lamellar structure around $t = 15\tau$, except in the region on top of the electrodes.

Right on top of the electrodes, the high field strength stabilizes a lying AB structure, where the high-ε component, B, is attracted to the high-field region at the substrate whereas the low-ε component, A, segregates to the free surface of the film. This lying AB structure differs from the initial BAB sandwich structure in the middle between the electrodes, but it is also frustrated by the thickness constraint. Thus, at this high voltage, a grain boundary between a lying AB structure on

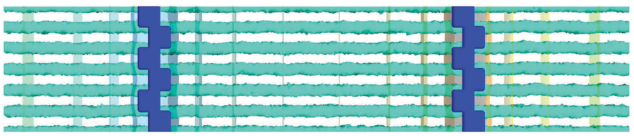

Fig. 4 Final state of the ordering on top of structured electrodes. The picture shows a view of the system from the bottom. The electrodes are shown in blue. Only the B domain with the higher dielectric constant is shown as cyan-colored stripes, the second domain is made invisible. Additional equipotential surfaces are presented to indicate the strength of the electric field in the film. The B domains register at the edges of the electrodes where the magnitude of the electric field is strongest.

top of the electrodes and a defect-free, registered and aligned, lamellar domain between the electrodes is formed.†

(iii) Fusion of the standing, registered and aligned lamellae on top of the electrodes

The high field strength on top of the electrodes stabilizes the lying AB structure against standing lamellae that do not suffer from the film-thickness frustration. Therefore, we gradually reduce the field strength to slowly allow the adjacent, standing lamellae in the middle between the electrodes to invade the top of the electrodes, while still maintaining the positional registration to the edges of the electrodes. Some residual voltage, however, is required to maintain the positional registration of the lamellae at the edges of the electrodes and allow a defect-free fusion of the standing lamellae from the left and the right sides. We have verified that a sudden and complete removal of the electric field is likely to result in defects during the fusion of the standing lamellar domains on top of the electrodes. At the final stage of the simulation, the lamellae are all fully oriented and aligned to the electrode edges, as shown in Fig. 4. This figure demonstrates that the high-ε B-lamellae perfectly align with the edges of the structured electrodes.

We emphasize that the temporal control of the external thermodynamic condition – here, the electric potential between the electrodes – during the three stages, encompassing the formation of the initial BAB sandwich structure, the reorientation into standing and registered lamellae between the electrodes, and the removal of the two grain boundaries at the electrodes, is critical. We refer to this strategy as process-directed self-assembly. The initial high electric field is required to align the lamellae in the middle of the film leads to parallel lamellae on top of the electrodes. If the electric field were switched off after the initial alignment step, the lamellae on top of the electrodes would have a high probability to misconnect, introducing defects on the electrodes. Instead, the electric field at the end of the process needs to register the lamellae, but also allow the lamellae to stand on top of the electrode. This synergistic, temporal interplay of field inhomogeneities, which are caused by the electrode edges and break the translational symmetry, and the homogeneous field between the electrodes and geometric confinement, which breaks the orientation symmetry, is the pivoting element of our strategy for simultaneous registration and alignment.

† We note that, in addition to the effect of the electric field, this orientation of the two lamellar domains at the grain boundary is preferred over the alternate configuration of lying AB domains on the electrodes and standing lamellae with normals along the x direction.[61]

5 Structure multiplication

Although the distance between the electrodes is large, one limitation of the example in the previous section is that the individual electrodes are structured on the same length scale, L_0, as the domain spacing of the BCP material. Similar to density multiplication in chemoepitaxy applications,[5] where chemical guiding patterns are spaced a small integer multiple, n, of the lamellar spacing apart, defect-free ordering does not require the registering of every lamella, and this structure multiplication is very attractive for fabricating suitable electrodes that direct the structure formation of the BCP material.

In order to illustrate structure multiplication, we choose a saw-tooth shape with an angle that is smaller than $\pi/4$ and a periodicity of $4L_0$ along the y-direction as the electrode geometry. The two electrodes are spaced $L_x/2 = 10L_0$ apart along the x-direction. The spatial inhomogeneities of the electric field of this type of electrode are shown in Fig. 5. The field is strongest at the edges of the electrodes. Although the field enhancement is smaller than for the previous electrode shape, we will demonstrate that it still suffices to register the BCP structure.

The ordering pathway, depicted in the top panel of Fig. 6, is similar to the registration and alignment mechanism of the electrode with a finer structure. Fig. 7 presents the details of the initial kinetics of structure formation. Again, in the very early stage, $t = 0.01\tau$, the inhomogeneities of the electric field at the electrodes acts like a preferential field that attracts the component, B, with the higher dielectric constant. This preference directs the spinodal microphase separation of the unstable, disordered structure at $\chi N = 18$. The spinodal ordering process leads to the formation a BAB-sandwich structure on top of the electrodes and, to a weaker extent, also in the region between the electrodes.

In the following, $t < 0.1\tau$, this BAB-sandwich structure extends away from the electrodes and pervades the entire film.

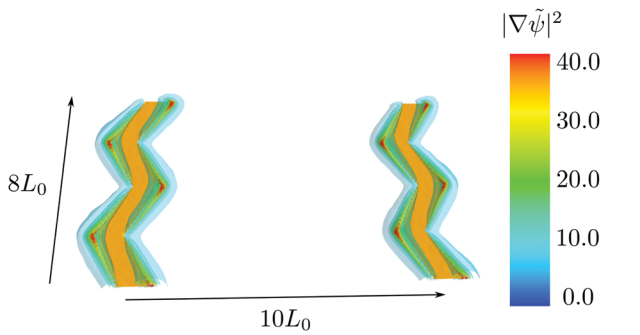

Fig. 5 Field inhomogeneities of a saw-tooth shaped electrode. The orange stripes denote the position of the electrodes. The semitransparent surfaces represent the strength of the inhomogeneities of the electric field $|\nabla\psi|^2$ with an applied potential of $\phi_{\text{electrode}} = \pm 10\tilde{\psi}$ to the electrodes.

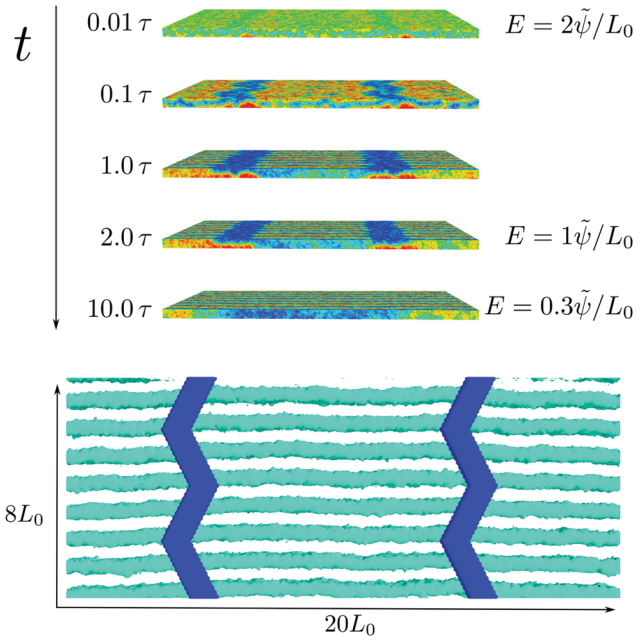

Fig. 6 The ordering process on top of a saw-tooth patterned electrode. (top) The images show a view at the system from the side at various times as indicated in the key. The strength of the electric field is denoted on the right. After the initial ordering process, which is presented in Fig. 7, the applied field is reduced, resulting in a defect-free, aligned and registered structure at $t = 10\tau$. (bottom) Bottom view of the final structure at $t = 10\tau$. The electrodes are shown in blue. Only the domain with the higher dielectric constant is depicted as teal stripes, the second domain is made invisible for clarity. Additional equipotential surfaces are depicted to indicate the strength of the electric field in the film. The high-ε domains register with the edges of the electrodes, where the electric field is strong.

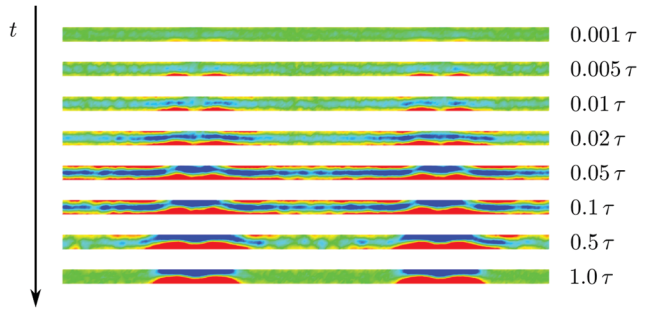

Fig. 7 Initial kinetics of the alignment process. The graphs present the averaged order parameter along the y-axis of the electrodes to illustrate the two-fold process at this stage. (i) At $t = 0.01\tau$ the inhomogeneities of the electric field at the electrodes attracts the component with the higher dielectric constant. Subsequently, this BAB-sandwich structure expands away from the electrodes, creating an unstable intermediate BAB-sandwich structure throughout the film. After $t = 0.1\tau$ this sandwich reorients and forms standing lamellae in the middle of the film. At $t = 1\tau$ this reorientation process of forming standing lamellae in the middle of the film is completed.

Whereas the homogeneous electric field in the middle between the electrodes does not exert a torque on the dielectric interfaces, the structure is highly frustrated because its natural thickness L_0 is significantly larger than the film thickness $3L_0/4$.

Thus, starting on top of the electrodes, the structure rearranges. The high field on top of the electrodes does not permit standing lamellae and the BAB-sandwich transforms to a lying AB structure. Between the electrodes, however, the electric field mainly points in the x-direction and thus favors lamellar normals in the yz-plane. Standing lamellae, with normal vectors along the y-direction, conform with the orientation effect of the electric field and do not suffer any frustration from the constraint film thickness. Thus aligned and standing lamellae form between the electrodes. Since the transformation from the BAB-sandwich structure to the aligned, standing lamellae begins from the vicinity of the electrodes, the field inhomogeneities register the positions of the domains. Because the periodicity of the electrodes along the y-direction is $4L_0$, the registration is a bit more complex as on every side of the electrode only every fourth lamella is registered onto an edge, and the outward edge at the other side of the electrode has a shift of $2L_0$. This leads to the registration of every second lamellae on one of the sides of the electrode. Thus, similar to the finely structured electrodes, at $t = \tau$ the structure consists of a periodic arrangement to two types of grains: (i) a lying AB structure on top of the electrodes and (ii) registered, aligned and standing lamellae between the electrodes.

Gradually reducing the voltage between the electrodes, the grain of lying AB lamellae, which is frustrated by the film-thickness constraint, shrinks and the standing lamellae expand and merge in turn, until a defect-free, aligned structure is formed across the entire film as demonstrated in the bottom panel of Fig. 6. The registration to the edges has some freedom because the angle of the kinks of this type of electrode is low.

This example of structure multiplication with sparse electrodes that are structured with the periodicity of $4L_0$ and are a distance $10L_0$ apart also demonstrates that the strategy is rather robust and does not depend, *e.g.*, on the fine details of the edges of the electrodes.

6 Conclusions

Using Single-Chain-in-Mean-Field simulations of a soft, coarse-grained model we have investigated the structure formation of lamella-forming diblock copolymers with dielectric contrast in an inhomogeneous electric field between structured electrodes. The electric field between the electrodes pervades the entire film and dictates the overall orientation of the block copolymer structure. This long-range character of the electric field distinguishes the guiding field from chemo- or graphoepitaxy. The structure of the electrodes gives rise to local field inhomogeneities and the concomitant dielectrophoretic forces register the position of the lamellar structure. Tailoring the time-dependence of the voltage, we have identified a pathway where a sandwich structure is initially formed at the electrodes, avoiding the formation of defects in the film between the electrodes. Subsequently, this structure is replaced by registered standing lamellae. This study illustrates (i) the ability of inhomogeneous electric fields to dictate both, orientational order and translational registration, and (ii) the benefits of tailoring the time-dependence of the field strength to direct the structure formation and avoid defect

formation in the initial stages. This study was performed solely using DC fields. An interesting additional option is to investigate the effect of alternating current (AC) fields. Within our coarse-grained model, we expect that the main results of this paper also apply for AC fields, if one replaces the local permittivity $\varepsilon(\mathbf{r})$ by its frequency-dependent version. We note that in our coarse-grained model, microscopic degrees of freedom of the segments are integrated out and, therefore, the response is limited to low frequencies. In cases that the frequency of the AC field is in the same order as the chain relaxation time, however, new pathways of defect removal may emerge. We hope that these simulations will inspire experimental studies.

Appendix: solving the Laplace equation in a thin film

Since the electric potential, $\psi(\mathbf{r})$, is computed during the update of the quasi-instantaneous fields after every Monte-Carlo step, the numerical strategy of solving the electrostatic Laplace equation, eqn (5), is critical. Due to the long-range character of the electric field, ψ extends below the BCP film into the substrate and far above into the vacuum. We consider the problem for a periodic unit of the electrodes in lateral directions, x and y, and impose a constant electric potential, $\psi = 0$, on an xy-plane at $z = \pm 30L_0$ far above and below the substrate surface.

The electric field of two flat, structured electrodes of non-circular cross section at $z = 0$ between two constant potential surfaces at $z = \pm 30L_0$ is solved numerically by a finite-difference scheme.[48] Fig. 8 demonstrates the procedure for two saw-tooth electrodes that are spaced $10L_0$ apart in x direction. The far-field resembles that of two parallel wires and the structure formation in the BCP film has only a negligible influence. Therefore we pre-compute the electric field in a large system, $L_z = 60L_0$ in the initial configuration of a disordered structure, extract the potential ψ on the xy-planes at $z_- = -0.5L_0$ and $z_+ = L_z + 0.5L_0$ above and below the BCP thin film, and use these potential values, $\psi_0(x,y,z_-)$ and $\psi_0(x,y,z_+)$, as time-independent boundary conditions for the subsequent simulation. This strategy significantly reduces the computational domain, in which ψ has to be calculated in each Monte-Carlo step. This introduces a small error as the electrostatic field for an ordered lamellar system deviates from that of a homogeneous mixture. We calculated the difference of the field $(\nabla\psi)^2$ at the boundary region for both cases and found that the maximal error, which is found on top of the electrodes has a magnitude of 4% compared to the field of a corresponding plate capacitor with the same distance and potential. The error drops below 1% at a distance of $1L_0$ to the electrodes. For comparison the field on the bottom of the polymer film is similar to the one of the corresponding plate capacitor, with an increasing perpendicular field component at higher distance to the bottom.

The simulation cell comprises more than a single lateral unit cell that is used to determine the boundary conditions. The boundary values, ψ_0, are periodically continued and the electric potential is computed in the domain $L_x \times L_y \times [z_-:z_+]$.

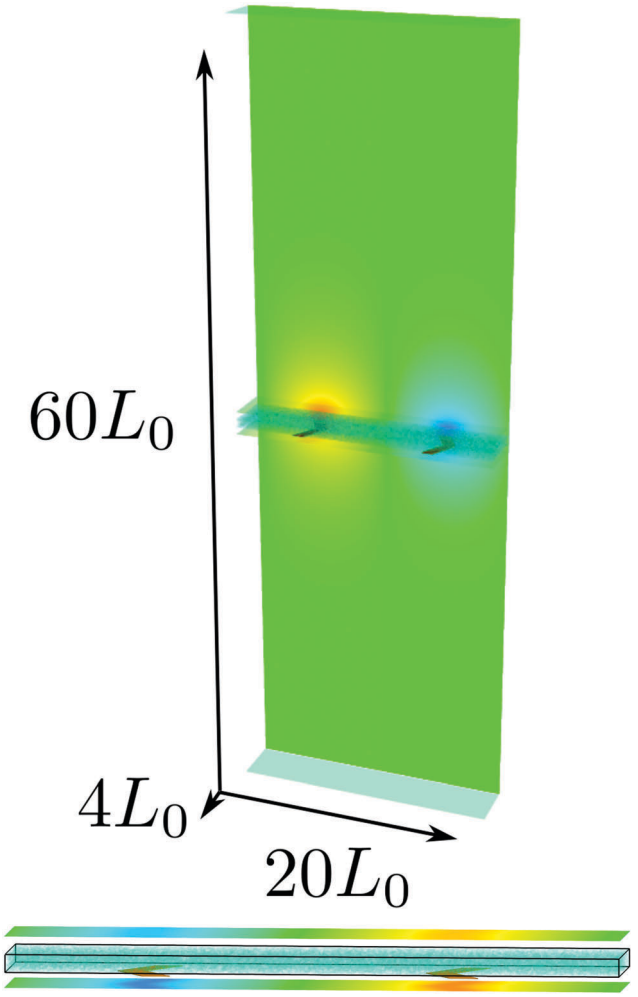

Fig. 8 (top) Electric field of two saw-tooth electrodes in the disordered BCP film (center), the solid substrate with dielectric constant $\varepsilon_s = 2$, and the vacuum above the film. At the very top and bottom there are neutral electrodes. The electrostatic potential, ψ, is depicted by the colors in the back xz plane. The two semi-transparent xy planes at $z_\pm$, above and below the BCP film, indicate the boundary values used to compute ψ_0 in the course of the simulation. (bottom) Magnification of the center part to demonstrate the electrostatic boundary conditions. The material on top of the polymer film is considered to be vacuum and below a material with $\varepsilon = 2.0$.

An iterative approach of using the electrostatic potential of the preceding step as a starting guess is employed that reduces the effort of keeping the electrostatic solution up to date to a couple of conjugate gradient steps of the order 10, and thus the computational extra costs due to the electrostatic interaction are equal to the costs of a Monte-Carlo sweep for the polymer system.

Acknowledgements

It is a great pleasure to thank Yoav Tsori for stimulating discussions and collaborations. Financial support by the German Science Foundation Mu1674/11 and the European Union FP7 under Grant agreement No. 619793 CoLiSA.MMP (Computational Lithography for Directed Self-Assembly: Materials, Models, and Processes) as well as generous access to supercomputers at the

GWDG Göttingen, the HLRN Hannover/Berlin, and the John von Neumann Center for Computing (NIC), Jülich, Germany, are gratefully acknowledged.

References

1 L. Leibler, *Macromolecules*, 1980, **13**, 1602–1617.
2 F. S. Bates and G. H. Fredrickson, *Phys. Today*, 1999, **52**, 32–38.
3 S. O. Kim, H. H. Solak, M. P. Stoykovich, N. J. Ferrier, J. J. de Pablo and P. F. Nealey, *Nature*, 2003, **424**, 411–414.
4 M. P. Stoykovich, M. Müller, S. O. Kim, H. H. Solak, E. W. Edwards, J. J. de Pablo and P. F. Nealey, *Science*, 2005, **308**, 1442–1446.
5 R. Ruiz, H. M. Kang, F. A. Detcheverry, E. Dobisz, D. S. Kercher, T. R. Albrecht, J. J. de Pablo and P. F. Nealey, *Science*, 2008, **321**, 936–939.
6 R. A. Segalman, H. Yokoyama and E. J. Kramer, *Adv. Mater.*, 2001, **13**, 1152–1155.
7 J. Y. Cheng, A. M. Mayes and C. A. Ross, *Nat. Mater.*, 2004, **3**, 823–828.
8 R. Ruiz, R. L. Sandstrom and C. T. Black, *Adv. Mater.*, 2007, **19**, 587–591.
9 I. Bita, J. K. W. Yang, Y. S. Jung, C. A. Ross, E. L. Thomas and K. K. Berggren, *Science*, 2008, **321**, 939–943.
10 A. K. G. Tavakkoli, K. W. Gotrik, A. F. Hannon, A. Alexander-Katz, C. A. Ross and K. K. Berggren, *Science*, 2012, **336**, 1294–1298.
11 S. B. Darling, *Prog. Polym. Sci.*, 2007, **32**, 1152–1204.
12 I. W. Hamley, *Prog. Polym. Sci.*, 2009, **34**, 1161–1210.
13 H. C. Kim, S. M. Park and W. D. Hinsberg, *Chem. Rev.*, 2010, **110**, 146–177.
14 A. P. Marencic, D. H. Adamson, P. M. Chaikin and R. A. Register, *Phys. Rev. E*, 2010, **81**, 011503.
15 A. V. M. Zvelindovsky, B. A. C. van Vlimmeren, G. J. A. Sevink, N. M. Maurits and J. G. E. M. Fraaije, *J. Chem. Phys.*, 1998, **109**, 8751.
16 A. V. M. Zvelindovsky and G. J. A. Sevink, *Europhys. Lett.*, 2003, **3**, 370–376.
17 D. J. C. Herr, *J. Mater. Res.*, 2011, **26**, 122–139.
18 K. Koo, H. Ahn, S. W. Kim, D. Y. Ryu and T. P. Russell, *Soft Matter*, 2013, **9**, 9059–9071.
19 H. Hu, M. Gopinadhan and C. O. Osuji, *Soft Matter*, 2014, **10**, 3867–3889.
20 W. H. Li and M. Müller, *Annu. Rev. Chem. Biomol. Eng.*, 2015, **6**, 187–216.
21 W. H. Li and M. Müller, *Prog. Polym. Sci.*, 2016, **54-55**, 47–75.
22 Z. R. Chen, J. A. Kornfield, S. D. Smith, J. T. Grothaus and M. M. Satkowski, *Science*, 1997, **277**, 1248–1253.
23 S. R. Ren, I. W. Hamley, P. I. C. Teixeira and P. D. Olmsted, *Phys. Rev. E*, 2001, **63**, 041503.
24 D. E. Angelescu, J. H. Waller, D. H. Adamson, P. Deshpande, S. Y. Chou, R. A. Register and P. M. Chaikin, *Adv. Mater.*, 2004, **16**, 1736–1740.
25 D. E. Angelescu, J. H. Waller, R. A. Register and P. M. Chaikin, *Adv. Mater.*, 2005, **17**, 1878–1881.
26 K. F. Luo and Y. L. Yang, *Polymer*, 2004, **19**, 6745–6751.
27 G. Arya, J. Rottler, A. Z. Panagiotopoulos, D. J. Srolovitz and P. M. Chaikin, *Langmuir*, 2005, **21**, 11518–11527.
28 M. W. Wu, R. A. Register and P. M. Chaikin, *Phys. Rev. E*, 2006, **74**, 040801.
29 J. Rottler and D. J. Srolovitz, *Phys. Rev. Lett.*, 2007, **98**, 175503.
30 A. P. Marencic, M. W. Wu, R. A. Register and P. M. Chaikin, *Macromolecules*, 2007, **40**, 7299–7305.
31 S. Pujari, M. A. Keaton, P. M. Chaikin and R. A. Register, *Soft Matter*, 2012, **8**, 5358–5363.
32 K. Amundson, E. Helfand, X. Quan, S. D. Hudson and S. D. Smith, *Macromolecules*, 1994, **27**, 6559–6570.
33 T. L. Morkved, M. Lu, A. M. Urbas, E. E. Ehrichs, H. M. Jaeger, P. Mansky and T. P. Russell, *Science*, 1996, **273**, 931–933.
34 B. Ashok, M. Muthukumar and T. P. Russell, *J. Chem. Phys.*, 2001, **115**, 1559.
35 A. Böker, H. Elbs, H. Hänsel, A. Knoll, S. Ludwigs, H. Zettl, V. Urban, V. Abetz, A. H. E. Müller and G. Krausch, *Phys. Rev. Lett.*, 2002, **89**, 135502.
36 A. V. Kyrylyuk, A. V. Zvelindovsky, G. J. A. Sevink and J. G. E. M. Fraaije, *Macromolecules*, 2002, **35**, 1473–1476.
37 T. Thurn-Albrecht, J. DeRouchey, T. P. Russell and R. Kolb, *Macromolecules*, 2002, **35**, 8106–8110.
38 A. Böker, H. Elbs, H. Hänsel, A. Knoll, S. Ludwigs, H. Zettl, A. Zvelindovsky, G. Sevink, V. Urban, V. Abetz, A. Müller and G. Krausch, *Macromolecules*, 2003, **36**, 8078–8087.
39 Y. Tsori and D. Andelman, *Macromolecules*, 2002, **35**, 5161–5170.
40 Y. Tsori, F. Tournilhac and L. Leibler, *Macromolecules*, 2003, **36**, 5873–5877.
41 M. W. Matsen, *Macromolecules*, 2006, **39**, 5512–5520.
42 M. W. Matsen, *Phys. Rev. Lett.*, 2005, **95**, 258302.
43 M. W. Matsen, *Soft Matter*, 2006, **2**, 1048–1056.
44 Y. Tsori, D. Andelman, C.-Y. Lin and M. Schick, *Macromolecules*, 2006, **39**, 289–293.
45 K. Schmidt, H. G. Schoberth, F. Schubert, H. Hänsel, F. Fischer, T. Weiss, G. Sevink, A. Zvelindovsky, A. Böker and G. Krausch, *Soft Matter*, 2007, **3**, 448–453.
46 Y. Tsori, *Macromolecules*, 2007, **40**, 1698–1702.
47 Y. Tsori, *Rev. Mod. Phys.*, 2009, **81**, 1471.
48 U. Welling, M. Müller, H. Shalev and Y. Tsori, *Macromolecules*, 2014, **47**, 1850–1864.
49 K. C. Daoulas and M. Müller, *J. Chem. Phys.*, 2006, **125**, 184904.
50 M. H. Müser and M. Müller, *J. Chem. Phys.*, 2015, **142**, 174105.
51 W. H. Li, P. F. Nealey, J. J. de Pablo and M. Müller, *Phys. Rev. Lett.*, 2014, **113**, 168301.
52 C. Harper, *Modern Plastics Handbook*, McGraw-Hill, 2000.
53 K. C. Daoulas, M. Müller, J. J. de Pablo, P. F. Nealey and G. D. Smith, *Soft Matter*, 2006, **2**, 573–583.
54 M. Müller, *J. Stat. Phys.*, 2011, **145**, 967–1016.
55 P. J. Rossky, J. D. Doll and H. L. Friedman, *J. Chem. Phys.*, 1978, **69**, 4628–4633.
56 M. Müller and K. C. Daoulas, *J. Chem. Phys.*, 2008, **129**, 164906.
57 P. E. Rouse, *J. Chem. Phys.*, 1953, **21**, 1272–1280.

58 H. Jung, S. Woo, S. Park, S. Lee, M. Kang, Y. Choe, J. G. Son, D. Y. Ryu, J. Huh and J. Bang, *Soft Matter*, 2015, **11**, 4242–4250.
59 S. M. Hur, V. Thapar, A. Ramirez-Hernandez, G. S. Khaira, T. Segal-Perez, P. A. Ricon-Delgalilio, W. Li, M. Müller, P. F. Nealey and J. J. de Pablo, *Proc. Natl. Acad. Sci. U. S. A.*, 2015, **112**, 14144.
60 M. Müller, B. Steinmüller, K. C. Daoulas, A. Ramirez-Hernandez and J. J. de Pablo, *Phys. Chem. Chem. Phys.*, 2011, **13**, 10491–10502.
61 D. Duque, K. Katsov and M. Schick, *J. Chem. Phys.*, 2002, **117**, 10315–10320.